




Synthesis of anatase TiO₂ microspheres and their efficient performance in dye-sensitized solar cell

V. Gowthambabu¹, Mrunal Deshpande², R. Govindaraj^{1,*} , V. K. Nithesh Krishna², M. Leela Charumathi², J. Manish Kumar², M. S. Dhilip Vignesh², R. Isaac Daniel¹, and P. Ramasamy¹

¹Department of Physics, SSN Research Centre, Sri Sivasubramaniya Nadar College of Engineering, Kalavakkam, Chennai, Tamil Nadu 603110, India

²Department of Electrical and Electronics Engineering, Sri Sivasubramaniya Nadar College of Engineering, Kalavakkam, Chennai, Tamil Nadu 603110, India

Received: 26 February 2021

Accepted: 27 August 2021

Published online:

1 October 2021

© The Author(s), under exclusive licence to Springer Science+Business Media, LLC, part of Springer Nature 2021

ABSTRACT

Nanomaterials play important role in performance of dye-sensitized solar cells. In this paper, highly phase pure anatase TiO₂ microspheres were synthesized using a low-cost hydrothermal route. Initially, X-ray diffraction studies and Raman spectroscopic analysis were carried out, and the formation of tetragonal structure of TiO₂ with the anatase phase was confirmed. The UV–Vis DRS studies showed the excellent reflectance and optical band-gap energy of 3.29 eV. The well-interconnected spherical nanoparticles with different sizes were examined by Field Emission Scanning Electron Microscopic analysis. The fabricated dye-sensitized solar cell (DSSC) composed of prepared TiO₂ microspheres as photoanode exhibited a higher power conversion efficiency (PCE) (η) of 5.4% as compared to commercial P25 with PCE of 3.6%. The higher J_{sc} (12.03 mA/cm²) in the fabricated DSSC due to efficient dye loading capacity and high light-scattering property was also observed.

1 Introduction

According to Nobel laureate Richard Smalley, the big challenge for the next 50 years is mainly in energy conservation and developments towards it to overcome environmental problems [1]. As compared to other renewable energy sources, solar energy proves to be most preferred source due to its continuous and abundant energy supply. The ‘Golden Triangle’ issues were considered to be an important thing to

develop photovoltaic (PV) technology. The issue contains decreasing the device cost, enhancing the power conversion efficiency, and improving the long-term stability [2]. Among three generations of solar cells, third-generation solar cells have the ability to rectify the aforementioned issues. Till date, the third-generation solar cells such as perovskite solar cells (PSC) ($\eta = 22\%$) [3], dye-sensitized solar cells (DSSC) ($\eta = 14\%$) [4], organic solar cells (OSC) ($\eta = 18\%$) [5], and quantum dot-sensitized solar cells (QDSSC)

Address correspondence to E-mail: isrogovindaraj@gmail.com

($\eta = 16\%$) [6] were employed due to their superior performance and cost efficiency. More recently, DSSCs have received great attention due to their lower cost, easy fabrication process, lightweight, and high efficiency. Till date, these cells have shown the maximum power conversion efficiency of 14.3% and 14.7% under 100 mW/cm² and 50 mW/cm², respectively [4]. The cutting edge of research mainly focuses on all DSSCs components such as semiconductor photoanode, highly electrocatalytic counter electrodes, sensitizers, and electrolytes. To achieve an excellent performance of photoanodes, larger surface area, fast electron transport kinetics, and large light-scattering effects are required [7]. TiO₂ is a wide band-gap semiconductor metal oxide and is effectively used in versatile applications like photocatalysis [8], Li-ion battery [9], hydrogen production [10], antireflective coatings [11], gas sensors [12], optical filters [13], water splitting [14], and photoelectrochemical solar energy conversion [15]. Due to its unique features such as the high surface area to absorb dye molecules, long-term stability, ease of availability, cost-affordability, non-toxic nature, compatible optical and electronic properties, it is specifically used as photoanode in DSSCs [16]. As compared to other photoanode materials like ZnO [17], SnO₂ [18], WO₃ [19], Nb₂O₅ [20], SrTiO₂ [21], Zn₂SnO₄ [22] and BaSnO₃ [23], the anatase TiO₂ photoanode exhibits the highest power conversion efficiency of about 14% [4]. Various nanostructures like nanotubes [24], nanowires [25], nanofibers [26], hollow spheres [27], and microspheres of TiO₂ [28–30] were effectively used as photoanode material. Among these aforementioned nanostructures, microspheres were extensively used in DSSC due to their larger surface area, large sphere diameter, superior dye adsorption ability, better light-scattering property, and efficient interconnection of nanospheres [31]. Several researchers have adopted various techniques to synthesize the microspheres using high-temperature hydro/solvothermal treatment [32, 33], electrospray preparation [34], low-temperature copolymer synthesis [35], template-free chemically induced self-transformation [36], and electrospun process [37].

In this investigation, the authors have synthesized well-interconnected TiO₂ microspheres (TiO₂ MS) by hydrothermal method and fabricated the DSSC using prepared TiO₂ as photoanode. The detailed structural and morphological properties were studied using

powder X-ray diffraction (XRD) analysis, Raman spectroscopic analysis, and field emission scanning electron microscopic (FESEM) analysis. UV–Vis spectroscopic analysis was carried out to study the optical properties, and the optical band-gap energy was found to be 3.29 eV. The fabricated DSSC performance was evaluated, and the PCE (5.4%) from J–V curves, IPCE (56%), and electron lifetime τ (25.24 ms) from EIS were obtained. It was noted that TiO₂ MS-based photoanode exhibits superior DSSC performance than P25-based photoanode due to its better light-scattering ability and electron transport kinetics.

2 Experimental section

2.1 Materials used

The following reagents or chemicals were used to prepare TiO₂ MS and fabrication of DSSCs without any further purifications. Fluorine-doped tin oxide (FTO, 8 Ω /square) substrates, Pluronic 123 (99%), Titanium tetraisopropoxide (99%), Acetylacetone (99%), and Polyoxyethylene (10) octyl phenyl ether (Triton-X-100) were purchased from Sigma Aldrich. Titanium tetrachloride (99%) was purchased from Spectrochem. Cis-diisothiocyanato-bis(2,2'-bipyridyl-4,4'-dicarboxylato) ruthenium (II) bis (tetrabutylammonium) (known as N719 dye), Platisol T/SP, and Iodolyte HI-30 were purchased from Solaronix SA, Switzerland, Tetrabutanol, Ethanol (99%), Hydrochloric acid (32%), and Acetonitrile were purchased from Merck.

2.2 Synthesis of TiO₂ microspheres

In this typical synthesis procedure, the hydrothermal method was adopted for synthesis of TiO₂ MS, and it is as shown in Fig. 1. Initially, 3 mL of absolute ethanol containing 0.2 g of pluronic 123 was stirred for 15 min, and it is termed as solution A for future reference. On the other hand, 1 mL of titanium tetraisopropoxide was added into solution B containing 0.7 mL of concentrated HCl and stirred for 15 min. Then, solution B was successively added into solution A and stirred for 30 min. The resultant solution was kept at ambient temperature without any disturbance for 24 h. After that, 12 mL of ethanol was added into the resultant mixture and transferred into Teflon-lined stainless steel autoclave for

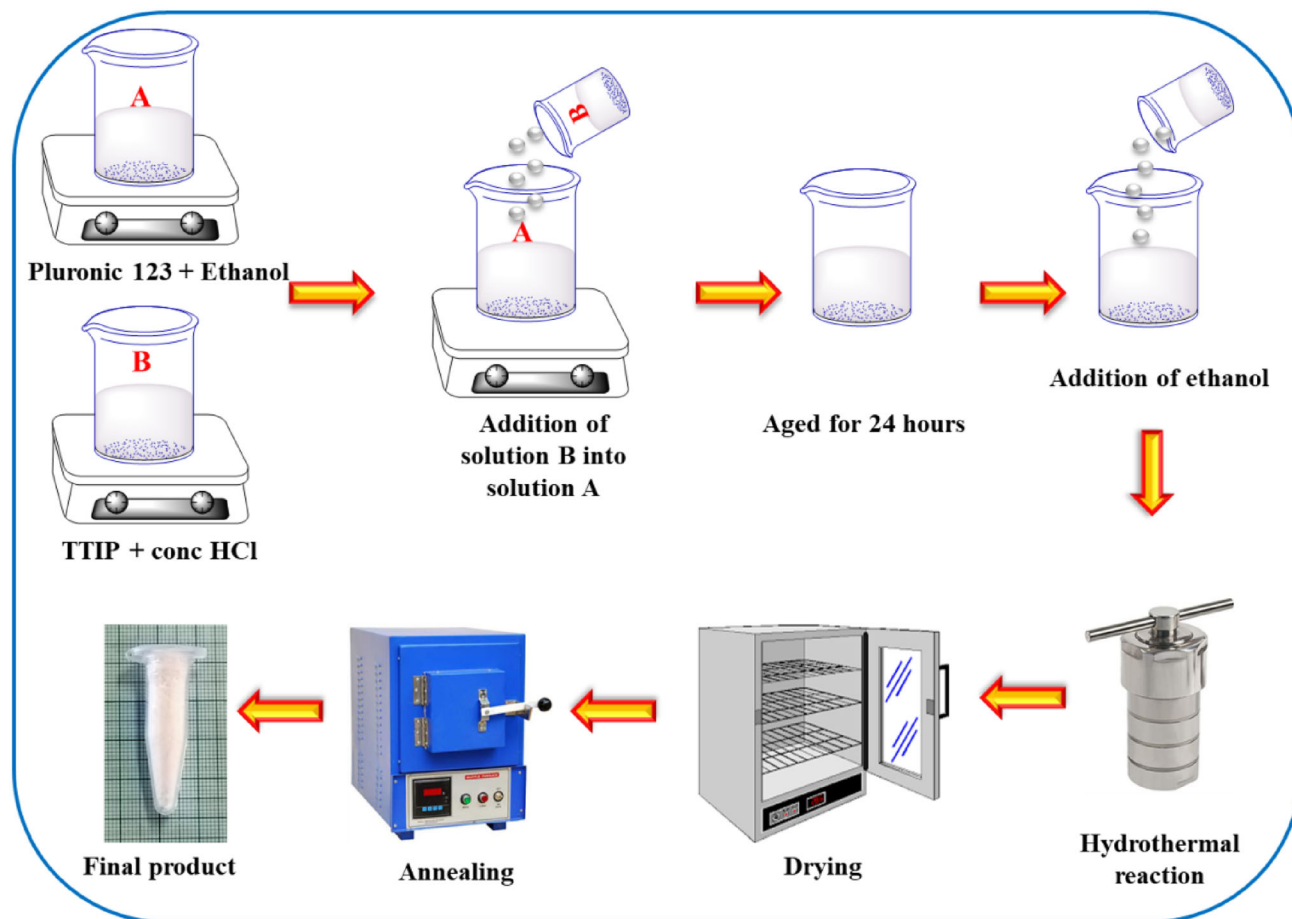


Fig. 1 Schematic representation for the synthesis of TiO_2 MS

hydrothermal reaction in a hot-air oven at $150\text{ }^\circ\text{C}$ for 24 h. The obtained product was rinsed several times with deionized water and ethanol to remove unwanted impurities. The resulting material was dried at $80\text{ }^\circ\text{C}$ for 24 h in a vacuum oven. The dried material was annealed at $500\text{ }^\circ\text{C}$ for 1 h in a muffle furnace.

2.3 Assembly of DSSC

Various steps were followed for assembly of DSSC: Initially, 1 g of prepared TiO_2 MS was mixed with 0.1 mL of acetylacetone and grounded well with the aid of agate mortar and pestle. The grounded products were stirred with a solution containing a 1:1 volume ratio of ethanol and water. 0.4 mL of Triton-X was added to the above solution to form a homogeneous TiO_2 paste. The FTO glass substrate was cleaned with deionized water and ethanol using an ultrasonication bath for 15 min. The cleaned FTO substrate was soaked with 0.2 M of aqueous TiCl_4

solution at $70\text{ }^\circ\text{C}$ for 30 min and rinsed with ethanol and heated at $500\text{ }^\circ\text{C}$ for 30 min (Pre- TiCl_4 treatment). After that, the doctor blade technique was adopted to coat TiO_2 paste on FTO substrate, and the coated FTO substrate was sintered at $500\text{ }^\circ\text{C}$ for 1 h to evaporate the binder materials in the coated films. The thickness of the sample coated on FTO substrate was found to be $\sim 14\text{ }\mu\text{m}$ using a thickness profilometer. The post- TiCl_4 treatment on sintered TiO_2 film was followed like pre- TiCl_4 treatment process. A similar process was followed to prepare commercial P25 film on FTO substrate. The resultant films were soaked in 0.5 mM of N719 dye in a 1:1 volume ratio of tertbutanol (10 mL) and acetonitrile (10 mL) solution for 24 h under dark conditions. The platinum (Pt) counter electrode was coated on another FTO substrate by doctor blade technique with Platisol T/SP as the platinum precursor and thermally decomposed at $400\text{ }^\circ\text{C}$ for 30 min. At last, the dye-adsorbed photoanode and Pt counter electrodes were

sandwiched together. To complete the device fabrication, a small amount of Iodolyte HI-30 as an aqueous electrolyte was injected in-between the two electrodes and the active area of the cell was found to be 0.25 cm^2 [38].

2.4 Characterization techniques

The crystallographic information of prepared TiO_2 MS was analyzed using a powder X-ray diffraction (EMPYREAN X-RAY DIFFRACTOMETER, PANALYTICAL, NETHERLANDS) instrument having a $\text{Cu-K}\alpha$ radiation wavelength of 1.5406 \AA . Micro-Raman measurements were carried out using (RENISHAW InVia Confocal Raman microscope, United Kingdom). Field Emission Scanning Electron Microscope (ZEISS, SIGMA, GHBM, GERMANY) was used to analyze the morphological properties of the prepared TiO_2 MS. The optical properties of the prepared material were analyzed using UV-Vis DRS (PerkinElmer, Lambda 35 spectrophotometer). The current density–voltage characteristics of fabricated DSSC were measured using Keithley digital source meter 2400 under 100 mW/cm^2 illumination coming from a solar simulator (UHE-16 equipped with a 150 W Xenon Arc lamp and an AM 1.5 filter, Scientech, Canada). The light intensity was calibrated with a standard crystalline silicon solar cell to carry out the J-V measurements. Incident photon-to-current conversion efficiency (IPCE) data were collected in the wavelength from 350 to 800 nm by using QE system (Enlitech, QE-R). The electrochemical impedance measurement of the fabricated DSSC was analyzed using an electrochemical workstation (FRA/VERSASTAT3, V3-500, Princeton Applied Research, USA) under the illumination at open-circuit voltage.

3 Results and discussions

3.1 X-ray diffraction analysis

Phase identification, crystalline features, and average crystallite size of hydrothermally synthesized TiO_2 MS and commercial TiO_2 (P25) were examined by powder XRD analysis, and the graphs are as shown in Fig. 2. From Fig. 2, it is observed that TiO_2 MS possesses a tetragonal crystal structure of an anatase phase with preferred (101) orientation at $2\theta = 25.32^\circ$.

All the diffraction peaks are well matched with JCPDS No: 21–1272 ($a = b = 3.785$, $c = 9.513$) with a crystallographic space group of $I4_1/amd$. The diffraction peaks located at 25.31° , 37.86° , 48.07° , 53.97° , 55.09° , 62.72° , 68.85° , 70.31° , and 75.15° were corresponding to (101), (004), (200), (105), (211), (204), (116), (220), and (215) crystal planes, respectively. No other additional diffraction peaks corresponding to metallic Ti and other impurity phases like rutile and brookite were observed. Hence, it is evident that synthesized material has pure phase and crystalline nature [28]. The commercial TiO_2 (P25) has a mixed phase of both anatase and rutile. In Fig. 2, the notations A and R represent anatase and rutile phase, respectively. The average crystallite size was found to be 18 nm with the aid of Debye–Scherrer formula, which is as follows:

$$D = \frac{k\lambda}{\beta \cos\theta} \quad (1)$$

where 'D' is the average crystallite size (nm), 'k' is the shape factor which corresponds to 0.9, ' λ ' is the wavelength of X-ray used (1.5406 \AA), ' β ' is the full width at half maximum of prominent diffraction peak (degree), and ' θ ' is the Bragg diffraction angle (degree) [39].

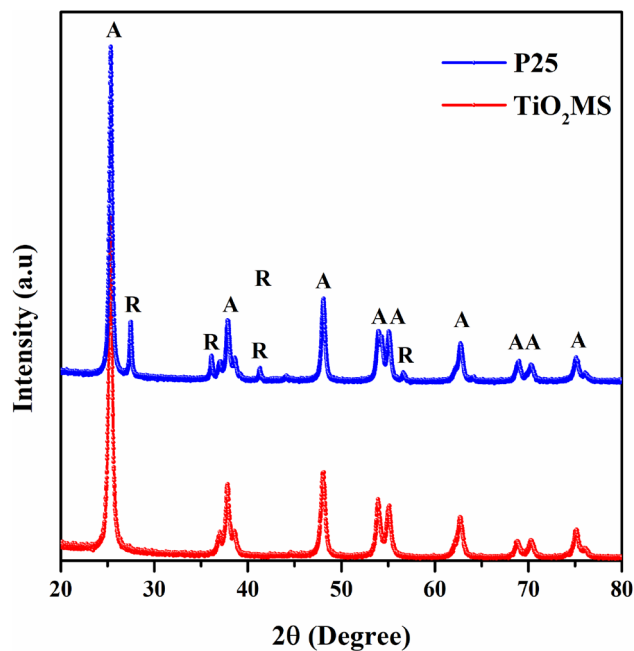


Fig. 2 Powder XRD pattern of TiO_2 MS

3.2 Raman analysis

Figure 3 shows the Raman spectra of synthesized TiO₂ MS. The Raman scattering peaks obtained at 144 cm⁻¹, 197 cm⁻¹, 397 cm⁻¹, 516 cm⁻¹, and 639 cm⁻¹ were ascribed to E_{1g}, E_{1g}, B_{1g}, A_{1g}, and E_{1g}-active vibrational Raman modes. The peaks at 144 cm⁻¹, 197 cm⁻¹, and 639 cm⁻¹ correspond to E_{1g} mode which are attributed to the symmetric stretching mode of the O–Ti–O bond. The B_{1g} and A_{1g} modes of peaks at 397 cm⁻¹ and 516 cm⁻¹ mainly correspond to symmetric and antisymmetric vibration-bending modes of O–Ti–O bond, respectively. Here, all the observed characteristics peaks belong to the typical anatase TiO₂ phase, and no other additional phases were observed from Raman spectra which are also in good agreement with XRD results [40–42].

3.3 UV–visible spectroscopic and dye desorption studies

To study the optical properties of the prepared TiO₂ MS, UV–Vis DRS spectroscopic measurements were carried out. Figure 4 shows diffused reflectance spectra of prepared TiO₂ microspheres which were

recorded in the wavelength range of 300 to 1100 nm. The prepared TiO₂ microspheres exhibit excellent reflectance which will enhance the light-scattering property. The optical band-gap energy of prepared TiO₂ microspheres was determined using Kubelka–Munk function method. The relation is given as follows:

$$F(R) = \frac{(1 - R)^2}{2R} = \frac{K}{S} \quad (2)$$

where F(R) is the Kubelka–Munk function and R is the reflectance. F(R) is directly proportional to absorption coefficient (K) and inversely proportional to scattering coefficient (S) [43]. To estimate the band-gap energy, the graph plotted between $h\nu$ and $(h\nu F(R))^2$ and the band-gap energy was found to be 3.29 eV which is in good agreement with bulk TiO₂.

To estimate the dye loading performance of TiO₂ MS and P25, N719 dye-adsorbed photoanodes were immersed in 30 ml of solution containing 0.1 M of NaOH solution and amount of desorbed dye molecules was characterized by UV–Vis spectroscopic analysis. Figure 5 shows the UV–Vis absorbance spectra of N719 dye and desorbed dye solutions from TiO₂ MS and P25 in NaOH solution. From this graph, it can be observed that the dye loaded on synthesized

Fig. 3 Raman spectrum of TiO₂ MS

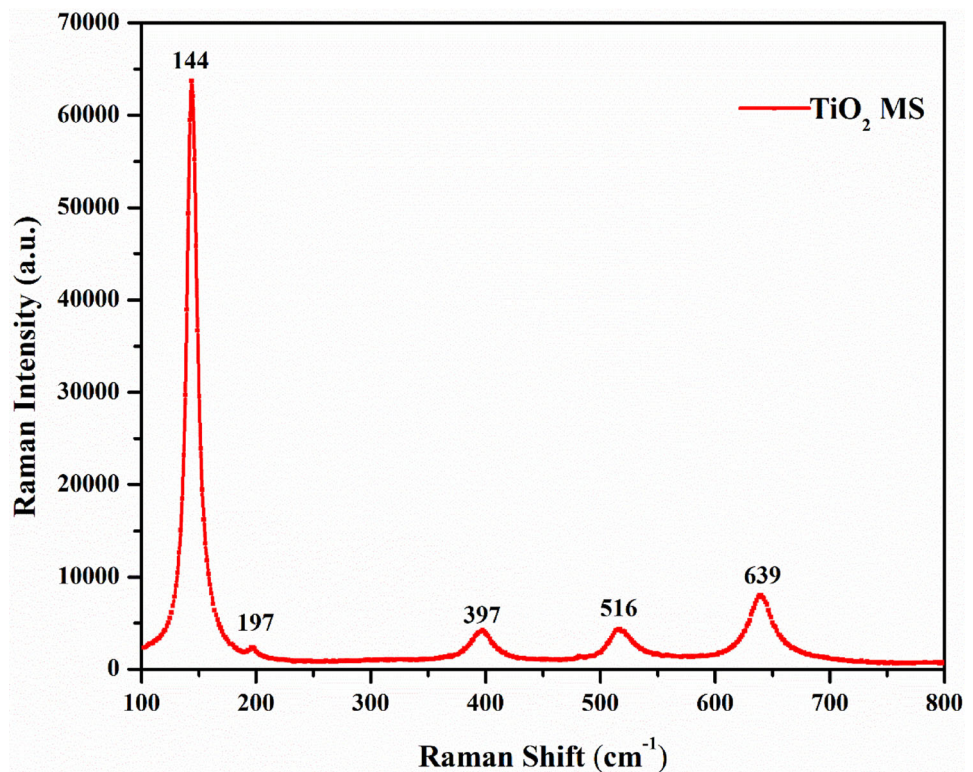
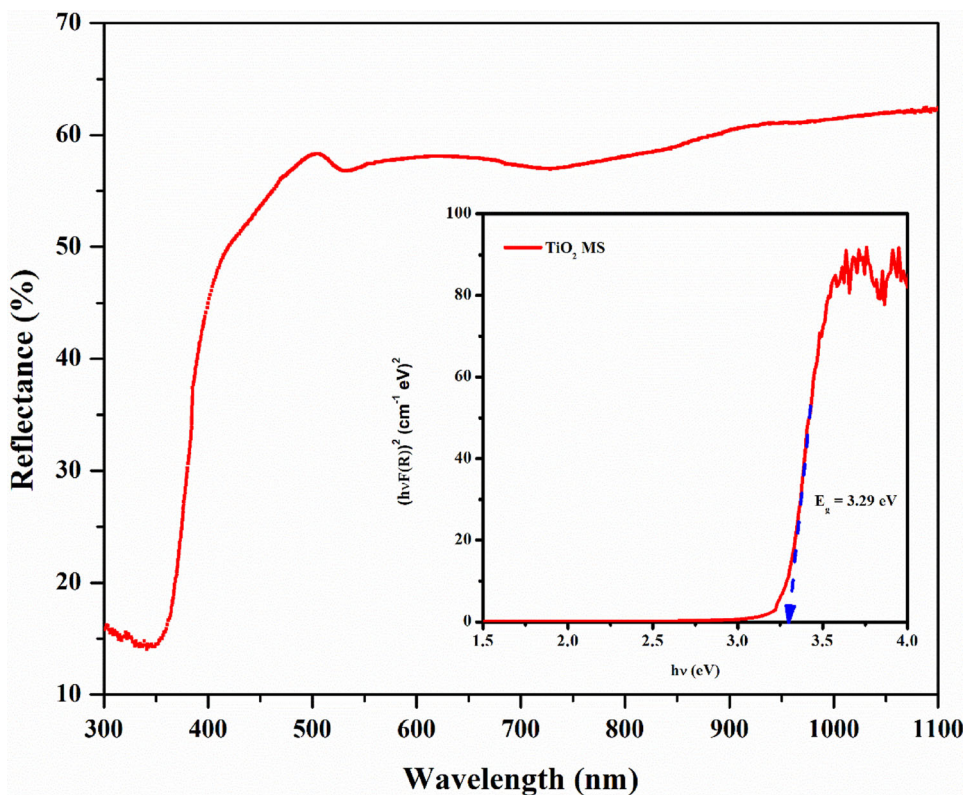


Fig. 4 UV–Vis DRS spectrum of TiO₂ MS and inset shows the Kubelka–Munk function plot



TiO₂ MS is much higher than P25 which will offer excellent current density.

3.4 FESEM analysis

The surface morphological properties of the prepared TiO₂ MS and commercial TiO₂ (P25) were

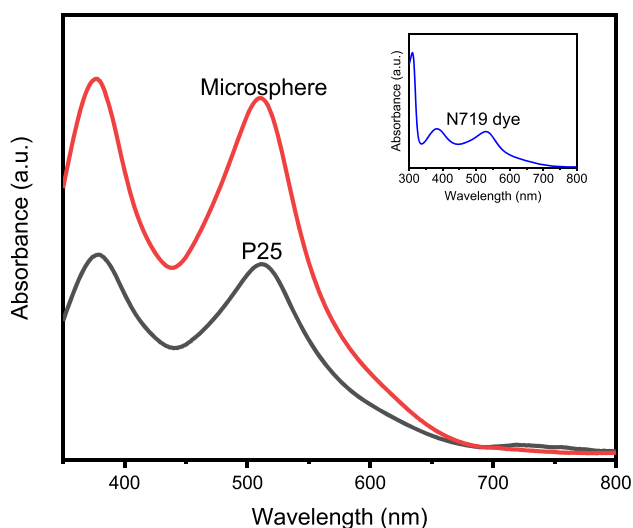


Fig. 5 UV–Vis absorption spectrum of N719 dye solution (inset) and after desorption of N719 dye from TiO₂ MS and P25 films

characterized by field emission scanning microscopic analysis, and the FESEM micrograph is shown in Fig. 6a and b. From this micrograph, the TiO₂ MS exhibits smoothly well-defined interconnected nanospheres of various sizes. These microspheres will provide better pathway for electron transport. There is some variation in the size of the microspheres. This could be due to some incomplete hydrolysis which occurred during the hydrothermal process resulting into the formation of irregular-shaped TiO₂ microspheres [44]. This can be tuned or controlled by optimizing experimental process parameters.

3.5 Photovoltaic performance of the fabricated dye-sensitized solar cell

Figure 7 shows the schematic representation of DSSC consisting of semiconductor metal oxide (TiO₂ MS) coated on FTO substrate sensitized with N719 ruthenium complex dye for absorbing visible light, I₃⁻/I⁻-based redox electrolytes for reducing oxidized dye and boosting the redox couple regeneration, a platinum counter electrode for collecting the electrons from the external circuit. According to the principle of DSSC, the voltage generated under the

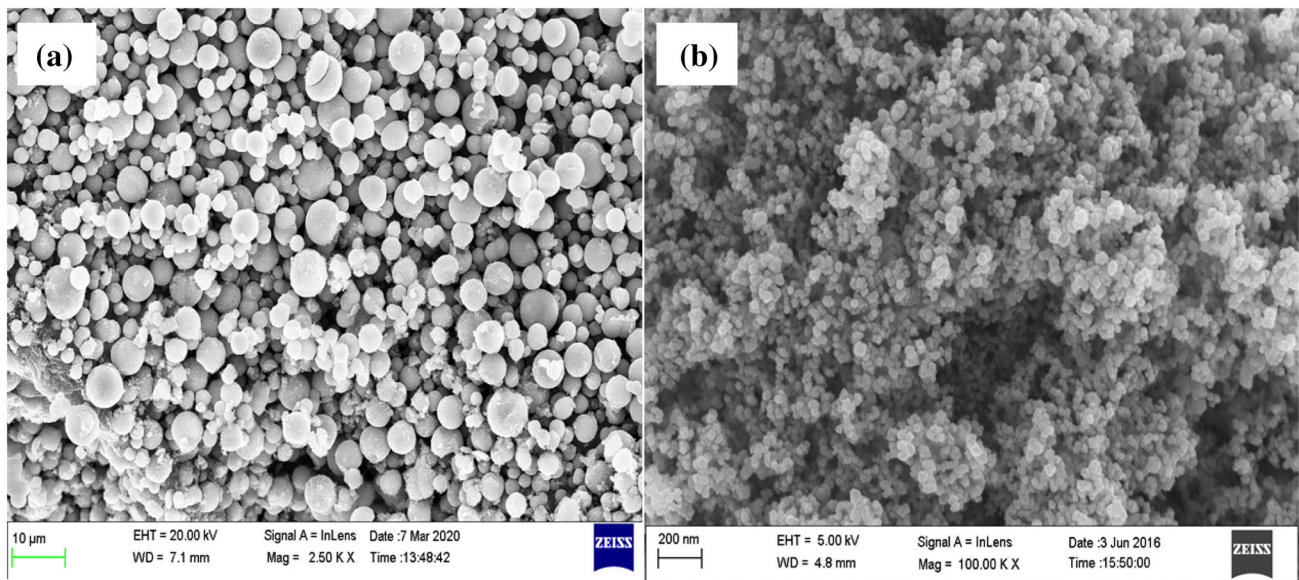


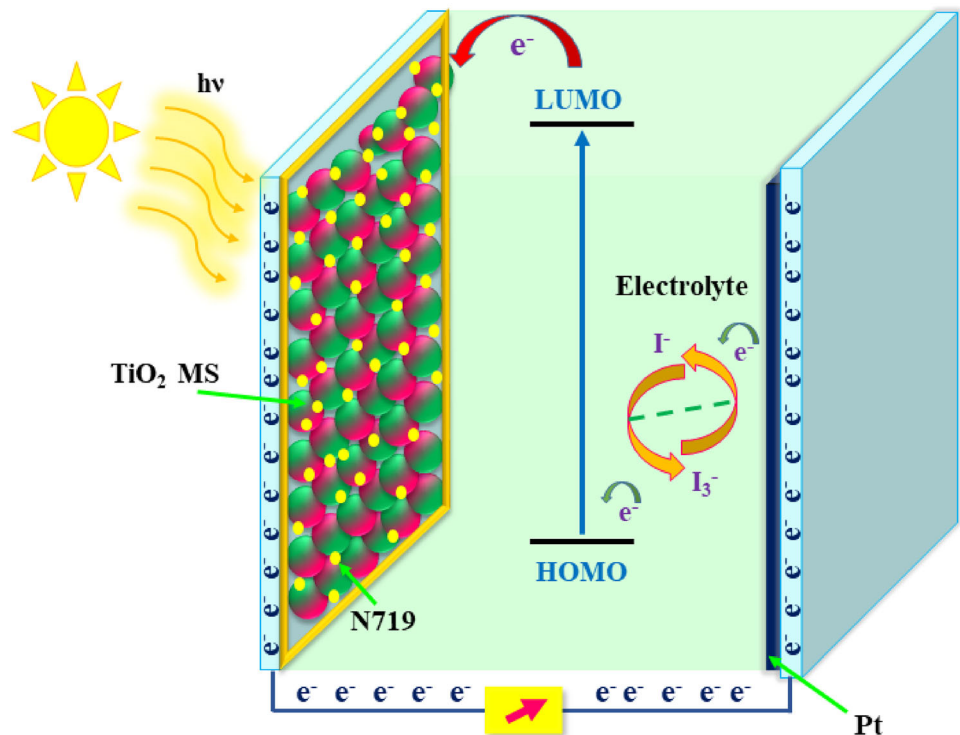
Fig. 6 FESEM micrograph of TiO_2 MS (a) and commercial P25 (b)

illumination of light radiation corresponds to the difference between the Fermi level of the electron in the binary semiconductor metal oxide and the redox potential of the electrolyte.

Figure 8 demonstrates the current density–voltage (J – V) characteristics of fabricated DSSC using prepared TiO_2 MS as photoanode sensitized with N719

dye for 24 h. The obtained solar cell parameters such as open-circuit voltage (V_{oc}), short-circuit current density (J_{sc}), fill factor (FF), and power conversion efficiency (η) are tabulated in Table 1. The fill factor (FF) and power conversion efficiency (η) can be expressed as follows:

Fig. 7 Schematic diagram of DSSC



$$FF = \frac{I_{max} \times V_{max}}{J_{sc} \times V_{oc}} \tag{3}$$

$$PCE(\eta) = \frac{J_{sc} \times V_{oc} \times FF}{P_{in}} \tag{4}$$

where V_{oc} and J_{sc} are open-circuit voltage (V) and short-circuit current density (mA/cm^2) of DSSC, respectively. V_{max} and I_{max} are the maximum voltage and current, respectively. P_{in} is the incident light power ($100 \text{ mW}/\text{cm}^2$) [41].

The results obtained for the fabricated device exhibit the short-circuit current density (J_{sc}) about $12.03 \text{ mA}/\text{cm}^2$, open-circuit voltage (V_{oc}) about 0.716 V , fill factor (FF) about 0.63 , and the power conversion efficiency (η) of 5.4% . At the same time, the device fabricated using P25 exhibits the short-circuit current density (J_{sc}) of about $9.64 \text{ mA}/\text{cm}^2$, open-circuit voltage (V_{oc}) of 0.612 V , fill factor about 0.59 , and the power conversion efficiency of about (η) 3.6% . Basically, the J_{sc} of the fabricated DSSC was estimated by the initial number of photo-generated electrons injected into the conduction band of TiO_2 photoanode, which is significantly influenced by the light-harvesting performance of the photoanode including the scattering effect of the photoanode

Table 1 The photovoltaic parameters of the fabricated device

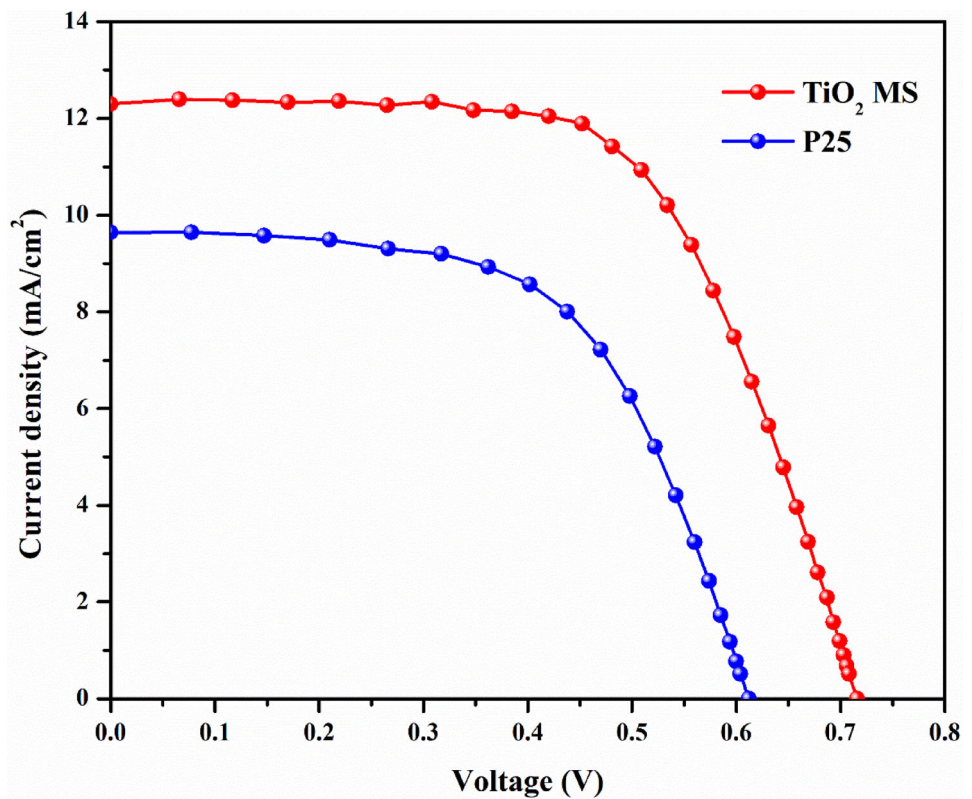
	V_{oc} (V)	J_{sc} (mA/cm^2)	FF	PCE (%)
TiO_2 MS	0.716	12.03	0.63	5.4
P25	0.612	09.64	0.59	3.6

structure and the overall dye loading amount [45]. In DSSC, the incident light loss occurs due to the backscattering of incident light in the FTO/ TiO_2 interface. The small underlayer consisting of small-sized TiO_2 nanoparticles or TiCl_4 treatments (pre or post) effectively showed the superior photocurrent density and the power conversion efficiency because of greater effect on electronic transport and causes the downward shift in the band edge [45, 46].

Incident photon-to-current conversion efficiency (IPCE) measurements were carried out to understand the performance of photoelectrodes which is shown in Fig. 9. The IPCE can be expressed as follows [47]

$$IPCE = \left(\frac{hc}{e}\right) \frac{J}{\lambda I_{light}} \tag{5}$$

Fig. 8 Current density—voltage curves of TiO_2 MS and commercial P25-based DSSCs



$$IPCE = 1240 \frac{J}{\lambda I_{\text{light}}} \quad (6)$$

where J is current density (mA/cm^2), λ is the incident light wavelength (nm), and I_{light} is the measured light intensity (mA/cm^2). Here, the authors have used wavelength ranging from 350 to 800 nm and the highest IPCE of about 56% was obtained at 520 nm for TiO_2 MS-based DSSC and about 39% was obtained at 520 nm for commercial P25. That mainly attributes to superior light scattering deriving from its characteristic photonic reflection effect which results in the higher J_{sc} in the fabricated device [45].

In DSSC, the electrochemical impedance spectroscopic analysis was used to understand the detailed charge transport and recombination kinetics of electrochemical properties. Figure 10 shows the Nyquist plot of a fabricated device which exhibits three semicircles corresponding to the diffusion of I_3^-/I^- electrolyte in lower-frequency region, charge transport at Pt/electrolyte interface in higher-frequency region, and the electron transport kinetics at dye/ TiO_2 /electrolyte interface in middle-frequency region [48]. Figure 11 demonstrates the corresponding bode plot of the fabricated device and the maximum mid-

frequency was observed at 6.31 Hz. The electron lifetime can be found to be 25.24 ms with the aid of the following relation and all EIS parameters are tabulated in Table 2.

$$\tau_e = \frac{1}{2\pi f_{\text{max}}} \quad (7)$$

where f_{max} is the peak frequency obtained from the bode plot [48].

Table 2 shows the comparative analysis of TiO_2 -based DSSC. Hun-Gi Jung et al. have used solvothermal approach to synthesis uniform-size TiO_2 microspheres, and they achieved PCE about 4.2% and current density about $8.7 \text{ mA}/\text{cm}^2$ using solid-state electrolyte [49]. Dubey et al. have achieved PCE about 1.5% and 2.1% for sol-gel and solvothermally derived TiO_2 nanoparticles [50]. Zn-doped TiO_2 microspheres exhibit PCE of 4.6% with current density of $14.38 \text{ mA}/\text{cm}^2$ [51]. Fang Xu et al. prepared photoanode using solvothermally derived uniform-sized TiO_2 microspheres and achieves PCE about 5.5% and $12.36 \text{ mA}/\text{cm}^2$ current density [52]. Mono-dispersed TiO_2 microspheres exhibit excellent current density about $14 \text{ mA}/\text{cm}^2$ and PCE about 5.7%, which were synthesized using chemical

Fig. 9 Incident photon-to-current conversion efficiency (IPCE) spectra of TiO_2 MS and commercial P25-based DSSC

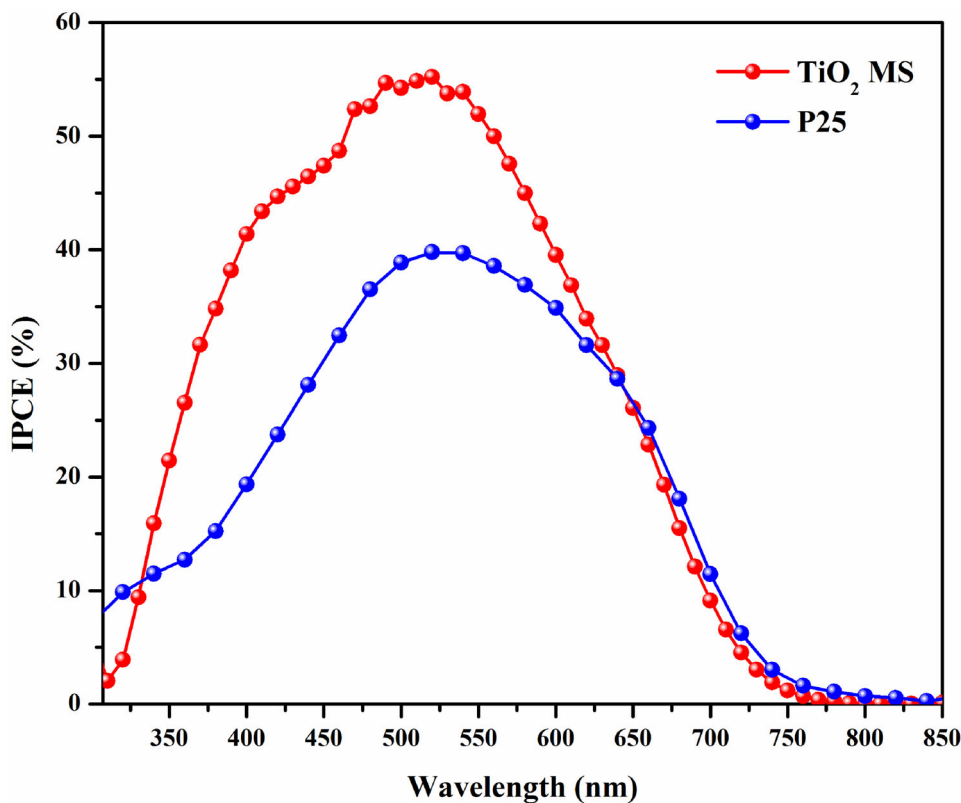


Fig. 10 Nyquist plot for TiO₂ MS-based DSSC

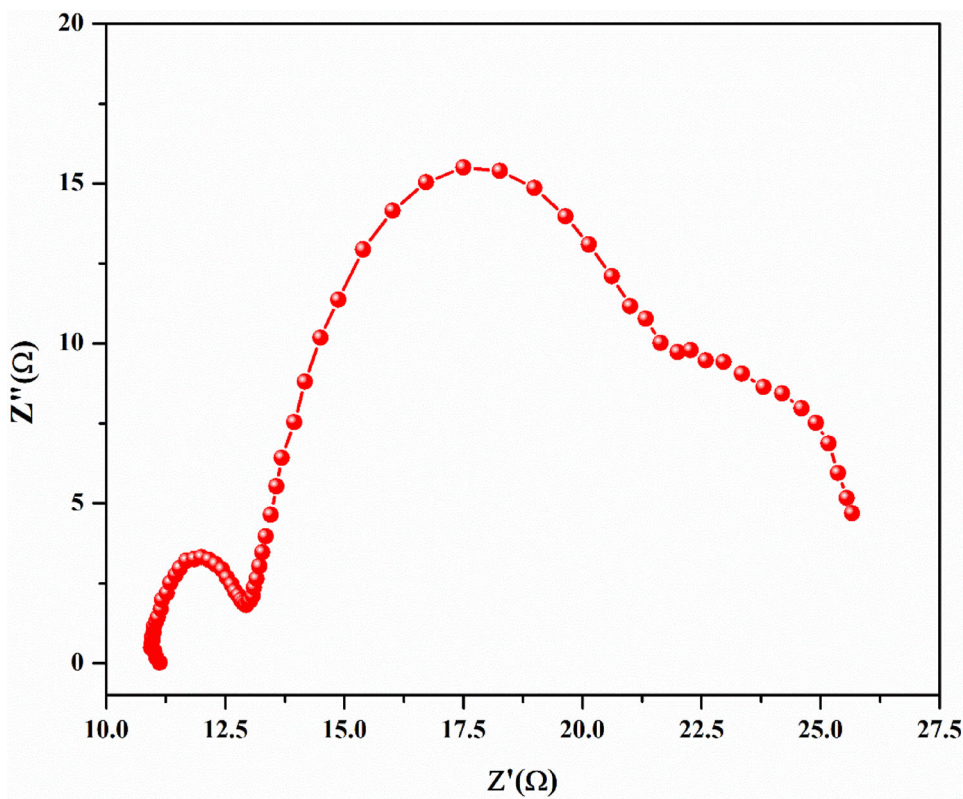
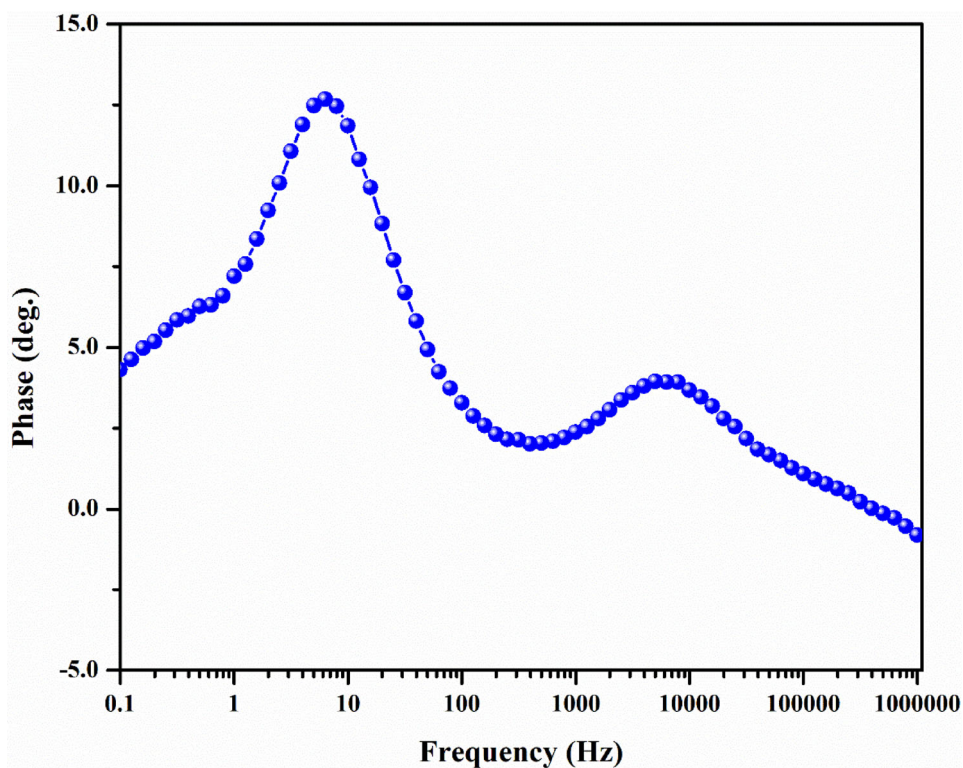


Fig. 11 Bode plot for TiO₂ MS-based DSSC



hydrolysis method [53]. In this present study, we have achieved the power conversion efficiency of

5.4% with excellent current density of 12.03 mA/cm² using hydrothermally synthesized irregular-sized

Table 2 EIS parameters of the fabricated device

Sample	R_s (Ω)	R_{ct1} (Ω)	R_{ct2} (Ω)	R_{ct3} (Ω)	f_{max} (Hz)	τ_c (ms)
TiO ₂ MS	11.12	01.82	08.05	04.66	6.31	25.24

Table 3 Comparison on photovoltaic parameters of TiO₂-based photoanode in DSSCs

Material	Synthesis method	Morphology	V_{oc} (V)	J_{sc} (mA/cm ²)	FF	PCE (%)	References
TiO ₂	Hydrothermal	Microspheres	0.716	12.03	0.63	5.4	This work
TiO ₂	Solvothermal	Microspheres	0.670	08.70	0.73	3.4	[49]
TiO ₂	Sol gel	Nanoparticles	0.640	03.90	0.7	2.1	[50]
TiO ₂	Sol gel	Nanoparticles	0.610	03.07	0.5	1.5	[50]
Zn-TiO ₂	Hydrolysis	Microspheres	0.73	14.58	0.44	4.63	[51]
TiO ₂	Solvothermal	microspheres	0.72	12.36	0.61	5.5	[52]
TiO ₂	Chemical hydrolysis	Monodisperse microspheres	0.72	14.60	0.54	5.7	[53]

TiO₂ microspheres. Here, the microspheres have huge impact on improvement in higher current density, better dye loading capability, and better pathway to movement of electrons (Table 3).

4 Conclusion

The TiO₂ microspheres were successfully synthesized using a one-step hydrothermal route. The pure anatase phase formation of TiO₂ MS was confirmed with the aid of XRD and Raman analysis. The average crystallite size was found to be 18 nm by adopting the Debye–Scherrer formula. The UV–Vis DRS results depict better reflectance and the optical band-gap energy was found to be 3.29 eV using Kubelka–Munk function plot. The DSSC was fabricated with the structure of FTO/TiO₂ MS – dye/redox couple electrolyte/Pt/FTO, and its efficiency was estimated under standard one sun illumination (100 mW/cm²). The photoanode made up of TiO₂ MS exhibits excellent power conversion efficiency of 5.4% than commercial P25 (3.6%). The improved PCE and J_{sc} could be due to superior light-scattering properties, electron transport properties, and pre-and post-treatment of TiCl₄ in Photoanode.

Acknowledgements

The authors gratefully acknowledge Sathyabama Institute of Science and Technology for providing access to their Raman and FESEM facilities.

Funding

SSN Trust (partially).

Data availability

Available data are transparent.

Declarations

Conflict of interest There are no conflicts to declare.

References

1. M.S. Ahmad, A.K. Pandey, N.A. Rahim, *Renew. Sust.* **77**, 89 (2019)
2. S. Mozaffaria, M.R. Nateghib, M.B. Zarandi, *Renew. Sust.* **71**, 675 (2017)
3. W.S. Yang, B.W. Park, E.H. Jung, N.J. Jeon, Y.C. Kim, D.U. Lee, S.S. Shin, J. Seo, E.K. Kim, J.H. Noh, S.I. Seok, *Science* **356**, 1376 (2018)
4. K. Kakiage, Y. Aoyama, T. Yano, K. Oya, J. Fujisawab, M. Hanaya, *ChemComm* **88**, 15894 (2015)
5. Q. Liu, Y. Jiang, K. Jin, J. Qin, J. Xu, W. Li, J. Xiong, J. Liu, Z. Xiao, K. Sun, S. Yang, X. Zhang, L. Ding, *Sci. Bull.* **65**, 272 (2020)
6. M. Hao, Y. Bai, S. Zeiske, L. Ren, J. Liu, Y. Yuan, N. Zarrabi, N. Cheng, M. Ghasemi, P. Chen, M. Lyu, D. He, J.H. Yun, Y. Du, Y. Wang, S. Ding, A. Armin, P. Meredith, G. Liu, H.M. Cheng, L. Wang, *Nat. Energy* **5**, 79 (2020)
7. X. Sun, Y. Liu, Q. Tai, B. Chen, T. Peng, N. Huang, S. Xu, T. Peng, X.Z. Zhao, *J. Phys. Chem. C* **116**, 11859 (2012)

8. A. Wold, *Chem. Mater.* **5**, 280 (1993)
9. H.G. Jung, S.W. Oh, J. Ce, N. Jayaprakash, Y.K. Sun, *Electrochim. Commun.* **11**, 756 (2009)
10. B. Liu, L.M. Liu, X.F. Lang, H.Y. Wang, X.W.D. Lou, E.S. Aydil, *Energy Environ. Sci.* **7**, 2592 (2014)
11. B.S. Richards, *Sol. Energy Mater. Sol. Cells* **79**, 369 (2003)
12. B. Karunakaran, P. Uthirakumar, S.J. Chung, S. Velumani, E.-K. Suh, *Mater. Charact.* **58**, 680 (2007)
13. M. Kitui, M.M. Mwamburi, F. Gaiho, C.M. Maghanga, *Int. J. Thin Fil. Sci. Tec.* **4**, 17 (2015)
14. S.U.M. Khan, M. Al-Shahry, W.B. Ingler Jr., *Science* **297**, 2243 (2002)
15. B. O'Regan, M. Gratzel, *Nature* **353**, 737 (1991)
16. Y.-Y. Yu, B.-X. Lei, M.-L. Xie, G.-L. Huang, W. Sun, Z.-F. Sun, *Adv Powder Technol* **26**, 1072 (2015)
17. S.S. Kanmani, K. Ramachandran, *J. Mater. Sci.* **48**, 2076 (2013)
18. E. Ramasamy, J. Lee, *J. Phys. Chem. C* **114**, 22032 (2010)
19. H. Zheng, Y. Tachibana, K.K. Zadeh, *Langmuir* **26**, 19148 (2010)
20. J.Z. Ou, R.A. Rani, M.H. Ham, M.R. Field, Y. Zhang, H. Zheng, P. Reece, S. Zhuiykov, S. Sriram, M. Bhaskaran, R.B. Kaner, K.K. Zadeh, *ACS Nano* **6**, 4045 (2012)
21. P. Jayabal, V. Sasirekha, J. Mayandi, K. Jeganathan, V. Ramakrishnan, *J. Alloys, Compd* **586**, 456 (2014)
22. J. Chen, L. Lu, W. Wang, *J. Phys. Chem. C* **116**, 10841 (2012)
23. N. Rajamanickam, P. Soundarajan, S.M. Senthil Kumar, K. Jayakumar, K. Ramachandran, *Electrochim. Acta* **296**, 771 (2019)
24. M.R. Venkatraman, N. Muthukumarasamy, P. Balraju, P. Selvakumar, V. Dhayalan, P. Arivalagan, *Int. J. Hydrog. Energy* **45**, 15441 (2020)
25. X. Feng, K. Zhu, A.J. Frank, C.A. Grimes, T.E. Mallouk, *Angew. Chem.* **124**, 2781 (2012)
26. M.S. Mahmoud, M.S. Akhtar, I.M.A. Mohamed, R. Hamdan, Y.A. Dakka, N.A.M. Barakat, *Mater. Lett.* **225**, 77 (2018)
27. X.Y. Ye, Y.H. Gu, H. Chen, Y.F. Cao, Y.Y. Liu, B.X. Lei, W. Sun, Z.F. Sun, *Adv. Powder Technol.* **30**, 2408 (2019)
28. Z.Q. Li, Y.P. Que, L.E. Mo, W.C. Chen, Y. Ding, Y. Mei Ma, L. Jiang, L.H. Hu, S.Y. Dai, *Appl. Mater. Interfaces* **7**, 10928 (2015)
29. J.D. Peng, C.M. Tseng, R. Vittal, K.C. Ho, *Nano Energy* **22**, 136 (2016)
30. P. Ilaiyaraja, T.K. Das, P.S.V. Mocherla, C. Sudakar, *Sol. Energy Mater. Sol. Cells* **169**, 86 (2017)
31. H. Tao, W. Chen, J. Wang, W. Ke, J. Wan, J. Wu, G. Fang, *Electrochim. Acta* **137**, 17 (2014)
32. X. Miao, K. Pan, Y. Liao, W. Zhou, Q. Pan, G. Tian, G. Wang, *J. Mater. Chem* **1**, 9853 (2013)
33. F. Sauvage, D. Chen, P. Comte, F. Huang, L.P. Heiniger, Y.B. Cheng, R.A. Caruso, M. Graetzel, *ACS Nano* **8**, 4420 (2010)
34. D. Hwang, H. Lee, S.Y. Jang, S.M. Jo, D. Kim, Y. Seo, D.Y. Kim, *Appl. Mater. Interfaces* **3**, 2719 (2011)
35. Y. Zhou, E.Y. Ding, W.D. Li, *Mater. Lett.* **61**, 5050 (2007)
36. J. Yu, J. Zhang, *Dalton Trans.* **25**, 5860 (2010)
37. G. Zhu, L. Pan, J. Yang, X. Liu, H. Sun, Z. Sun, *J. Mater. Chem.* **22**, 24326 (2012)
38. R. Govindaraj, N. Santhosh, M.S. Pandian, P. Ramasamy, *Appl. Surf. Sci.* **449**, 166 (2018)
39. S.S. Kanmani, N. Rajkumar, K. Ramachandran, *Int. J. Nanosci.* **10**, 227 (2011)
40. M.R. Venkatraman, N. Muthukumarasamy, S. Agilan, V. Asokan, D. Velauthapillai, *Mater. Res. Bull.* **97**, 351 (2018)
41. R. Govindaraj, N. Santhosh, M.S. Pandian, P. Ramasamy, M. Sumita, *J. Mater. Sci.: Mater. Electron.* **29**, 3736 (2018)
42. X. Tao, P. Ruan, X. Zhang, H. Sun, X. Zhou, *Nanoscale* **8**, 3539 (2015)
43. T. Amutha, M. Rameshbabu, S.S. Florence, N. Senthilkumar, I.V. Potheher, K. Prabha, *Res. Chem. Intermed.* **45**, 1929 (2019)
44. T.Z. Ren, Z.Y. Yuan, B.L. Su, *Chem. Phys. Lett* **170**, 374 (2003)
45. C. Ma, L. Wang, Z. Guo, Y. Lv, W. Chen, H. Ming, P. Ma, J. Wang, *Colloids Surf. A* **538**, 94 (2018)
46. S.D. Liu, Y.K. Ren, Z. Zhou, W.C. Chen, Z.Q. Li, F.L. Guo, L.-E. Mo, J.H. Wu, L.H. Hu, S.Y. Dai, *Adv. Powder Technol.* **329**, 225 (2019)
47. N. Rajamanickam, K. Ramachandran, *J. Colloid Interface Sci.* **580**, 407 (2020)
48. Z. Ge, C. Wang, Z. Chen, T. Wang, T. Chen, R. Shi, S. Yu, J. Liu, *Mater. Res. Bull.* **135**, 111148 (2021)
49. H.G. Jung, S. Nagarajan, Y.S. Kang, Y.K. Sun, *Electrochim. Acta* **848**, 89 (2013)
50. R.S. Dubey, K.V. Krishnamurthy, S. Singh, *Results Phys.* **102390**, 14 (2019)
51. Y. Zhang, L. Wang, B. Liu, J. Zhai, H. Fan, D. Wang, Y. Lin, T. Xie, *Electrochim. Acta* **6517**, 56 (2011)
52. F. Xu, X. Zhang, Y. Wu, D. Wu, Z. Gao, K. Jiang, *J. Alloys, Compd* **227**, 574 (2013)
53. Z. Zhu, C. Zhu, H. Liu, Y. Wu, G. Chen, T. Lv, *Appl. Surf. Sci.* **301**, 308 (2014)

Publisher's Note Springer Nature remains neutral with regard to jurisdictional claims in published maps and institutional affiliations.